

# **Ultrafast Spectroscopy of Plasmons and Free Carriers** in 2D MXenes

Erika Colin-Ulloa, Andrew Fitzgerald, Kiana Montazeri, Javery Mann, Varun Natu, Ken Ngo, Joshua Uzarski, Michel W. Barsoum, and Lyubov V. Titova\*

2D MXenes have diverse and chemically tunable optical properties that arise from an interplay between free carriers, interband transitions, and plasmon resonances. The nature of photoexcitations and their dynamics in three different members of the MXene family, Ti<sub>3</sub>C<sub>2</sub>, Mo<sub>2</sub>Ti<sub>2</sub>C<sub>3</sub>, and Nb<sub>2</sub>C, are investigated using two complementary pump-probe techniques, transient optical absorption, and time-resolved terahertz (THz) spectroscopy. Measurements reveal pronounced plasmonic effects in the visible and near-IR in all three. Optical excitation, with either 400 or 800 nm pulses, results in a rapid increase in lattice temperature, evidenced by a pronounced broadening of the plasmon mode that presents as a plasmon bleach in transient absorption measurements. Observed kinetics of plasmon bleach recovery provide a means to monitor lattice cooling. Remarkably slow cooling, proceeding over hundreds of picoseconds to nanoseconds time scales, implies MXenes have low thermal conductivities. The slowest recovery kinetics are observed in the MXene with the highest free carrier density, viz. Ti<sub>3</sub>C<sub>2</sub>, that supports phonon scattering by free carriers as a possible mechanism limiting thermal conductivity. These new insights into photoexcitation dynamics can facilitate their applications in photothermal solar energy conversion, plasmonic devices, and even photothermal therapy and drug delivery.

1. Introduction

MXenes are an emergent class of the 2D transition metal carbides, nitrides, carbonitrides or borides, with a general formula  $M_{n+1}X_nT_2$ , where M is a metal, X is carbon, nitrogen or boron,

E. Colin-Ulloa, A. Fitzgerald, J. Mann, L. V. Titova Department of Physics Worcester Polytechnic Institute Worcester, MA 01609, USA E-mail: Ititova@wpi.edu

K. Montazeri, V. Natu, M. W. Barsoum Department of Materials Science and Engineering Drexel University

Philadelphia, PA 19104, USA

V. Natu

Physical/Materials Chemistry Division CSIR-National Chemical Laboratory Dr Homi Bhabha Road, Pune 411008, India

K. Ngo, J. Uzarski US Army DEVCOM Soldier Center Natick, MA 01760, USA

The ORCID identification number(s) for the author(s) of this article can be found under https://doi.org/10.1002/adma.202208659.

DOI: 10.1002/adma.202208659

and n = 1, 2, 3 or 4, and  $T_2$  denotes surface terminations such as -OH, -O, and/ or -F. MXenes are so-called for being principally derived by selectively etching the A-group (mostly Al) layers from the MAX-phases. They are distinct among 2D materials in that they are intrinsically metallic, easily processable in water, and have, in their short twelve-year history, displayed an array of unique properties such as record volumetric capacitances and conductivities, optical nonlinearities, and high laser damage thresholds.[1-6] While their potential to revolutionize energy storage and act as flexible electrodes rightfully attracted much attention, MXenes also hold promise as candidates in photonic and optoelectronic devices such as electromagnetic interference, EMI, shields, optical and terahertz (THz) switches, modulators, wavelength converters, and detectors.<sup>[7–15]</sup> The optical properties of MXenes are diverse<sup>[16]</sup> and can be tailored by chemical composition, structure, and/or mor-

phology.<sup>[17,18]</sup> Their optical propertie scarise from a complicated interplay between free carriers, interband transitions as well as plasmon modes that occur in the visible and near-IR spectral ranges.<sup>[16,18,19]</sup> MXene plasmonic properties in particular are intriguing; while there is still much to be learned about the nature and properties of plasmons in different MXenes, localized surface plasmon resonances (LSPR) have already been hypothesized to underly efficient conversion of light to heat, saturable absorption in the visible and at telecommunication wavelengths, and high-performance photodetectors.<sup>[13,20–23]</sup>

In this work, we investigate the nature and dynamics of photoexcitations in three different members of the MXene family, viz.  $Ti_3C_2$ ,  $Mo_2Ti_2C_3$ , and  $Nb_2C$ . We use two complementary pump-probe techniques to uncover the effects of optical excitations. The first is transient optical absorption, TA, that characterizes the effects on the optical properties in the visible and near-IR range, where LSPR features are dominant. The second, time-resolved THz spectroscopy (TRTS) measurements provide information about the dynamics of free charge carriers. The MXenes chosen here represent a broad range of electronic and optical properties.  $^{[16]}$  As recent studies have uncovered, the most well-studied MXene,  $Ti_3C_2$ , is metallic with a high free carrier density ( $\approx 10^{22}$  cm $^{-3}$ ) and exhibits a pronounced LSPR extinction peak in the near-IR, in 750–800 nm range.  $^{[16,18,24]}$  On

ADVANCED MATERIALS

www.advmat.de

the other hand, Mo<sub>2</sub>Ti<sub>2</sub>C<sub>3</sub> combines two transition metals, Mo and Ti. It is also metallic but has a carrier concentration that is as much as two orders of magnitude lower than Ti<sub>3</sub>C<sub>2</sub>.<sup>[25]</sup> Free carrier density in the third investigated MXene, Nb<sub>2</sub>C, is even lower since its DC sheet conductivity is undetectable by a handheld multimeter.[16] Both Mo- and Nb-containing MXenes have been previously reported to have broad extinction feature in the visible and near-IR range, however, the origin of the observed optical transitions has not yet been clarified.<sup>[16]</sup> Our goal is to uncover the nature and dynamics of photoexcitations in these MXenes and elucidate the origin of the observed optical transitions. We demonstrate that all three 2D materials exhibit pronounced plasmonic effects in the visible and near-IR. Optical excitations with either 400 or 800 nm laser pulses create hot photocarrier distribution in all three MXenes, which rapidly transfers excess energy to the crystal lattice, in full agreement with reports of nearly perfect (100%) internal light-to-heat conversion efficiency, [23,26,27] and results in pronounced broadening of the plasmon modes. TA provides a means to track subsequent lattice cooling by monitoring the plasmon resonance over sub-picoseconds to nanoseconds time scales. We observe unusually slow lattice cooling, proceeding over hundreds of picoseconds to nanoseconds, compared to tens of picoseconds in conventional plasmonic materials, [28-30] indicating a low thermal conductivity in MXene films. Correlation between the instantaneous carrier density and the lattice cooling rate also supports strong carrier-phonon scattering as a possible mechanism behind the low thermal conductivities in MXenes.[31] These new findings shed new light into the dynamics of photoexcitations, as well as, into thermal relaxation in MXenes, and are important for MXene-based photonic and photothermal devices for energy generation, EM and biomedical applications.

## 2. Results

We have investigated transient changes in the optical and electronic properties of Ti<sub>3</sub>C<sub>2</sub>, Mo<sub>2</sub>Ti<sub>2</sub>C<sub>3</sub>, and Nb<sub>2</sub>C MXene films in response to UV (400 nm) and near-IR (800 nm) pulsed excitations. Preparation of the films from their colloidal suspensions are described in detail in the Experimental Section. For optical measurements, the films were produced by depositing a drop of colloid suspension onto a fused quartz substrate. The thicknesses of the resulting films, as determined by profilometry, were 56  $\pm$  2 nm for Ti<sub>3</sub>C<sub>2</sub>, 64  $\pm$  10 nm for Mo<sub>2</sub>Ti<sub>2</sub>C<sub>3</sub>, and 164  $\pm$ 20 nm for Nb<sub>2</sub>C. X-ray photoelectron spectroscopy (XPS) was used to characterize the bonding structure and surface chemistry of the three MXenes (Figure S1 and Tables S1-S3, Supporting Information). Based on XPS analysis, described in detail in Supporting Information, Mo<sub>2</sub>Ti<sub>2</sub>C<sub>3</sub> and Nb<sub>2</sub>C surfaces were mostly terminated with -OH and -O groups. The Ti<sub>3</sub>C<sub>2</sub> film also featured a significant number of -F surface groups.

**Figure 1** shows the static and TA of the  $\rm Ti_3C_2$  film. Static absorbance (Figure 1a,b) shows a prominent, broad absorbance peak at ≈750 nm (1.65 eV), consistent with previous literature reports that have ascribed this feature to an optically active LSPR. [16,32] Following excitation with a 400 nm, 50 fs pulse, we observe a pronounced suppression of optical absorption that is centered at 1.65 eV, coinciding in energy with the peak in static

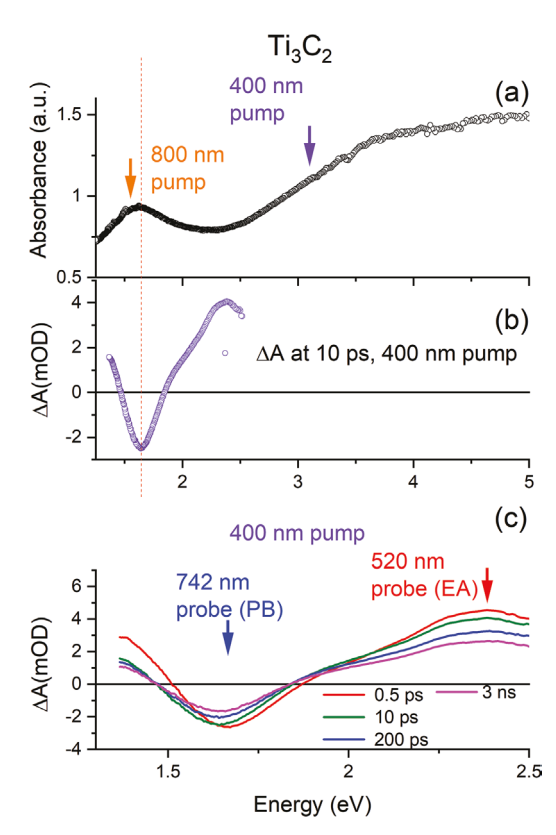


**Figure 1.**  $Ti_3C_2$ . a) UV–vis absorbance. Dashed line indicates presumed plasmon. b) Transient absorbance 10 ps after excitation with 400 nm pulse. c) Transient absorbance at four different times after excitation.

absorbance. This suppression, or bleach, appears in transient absorption,  $\Delta A$ ,  $(\Delta A = A(t) - A_0$ , where  $A_0$  is absorbance before excitation and A(t) is the absorbance at time t after the excitation with a laser pulse) as the plasmon band broadens when the laser pulse excites hot electrons that heat the entire electron gas by electron-electron scattering. The bleach eventually recovers as excess energy is dissipated by electron-phonon coupling and phonon transport, or heat diffusion, as discussed below. We, therefore, assign this transient feature to LSPR bleach (labeled PB in Figure 1c). In addition to PB, we also find enhanced absorption at energies >1.8 eV. This observed enhancement occurs largely due to the same broadening of the LSRP peak manifest in the PB feature. However, it may also feature contributions from the optical absorption by the charge carriers promoted to the excited states by the laser pulse, and a comparison of the kinetics of its recovery to that of PB can shed light on its nature. Here, we label it enhanced absorption, EA (Figure 1c). TA spectra at different times after excitation, as long as 3 ns (Figure 1c), show that both of these features are long-lived, and decay slowly without appreciable changes in the spectral shape save for an initial small red-shift between 0.5 and 10 ps that is in part a measurement artifact due to the spectral chirp of the probe pulse.

The same measurements on  $Mo_2Ti_2C_3$  films are shown in **Figure 2**. Previous studies have demonstrated a broad extinction peak in the blue-green portions of the spectrum.<sup>[16]</sup> Here, we observe this feature as well, as can be seen in Figure 2a. The center of this band is at  $\approx 520$  nm, or  $\approx 2.38$  eV (see dashed

-and-conditions) on Wiley Online Library for rules of use; OA articles are governed by the applicable Creative Commons License

www.advancedsciencenews.com

www.advmat.de

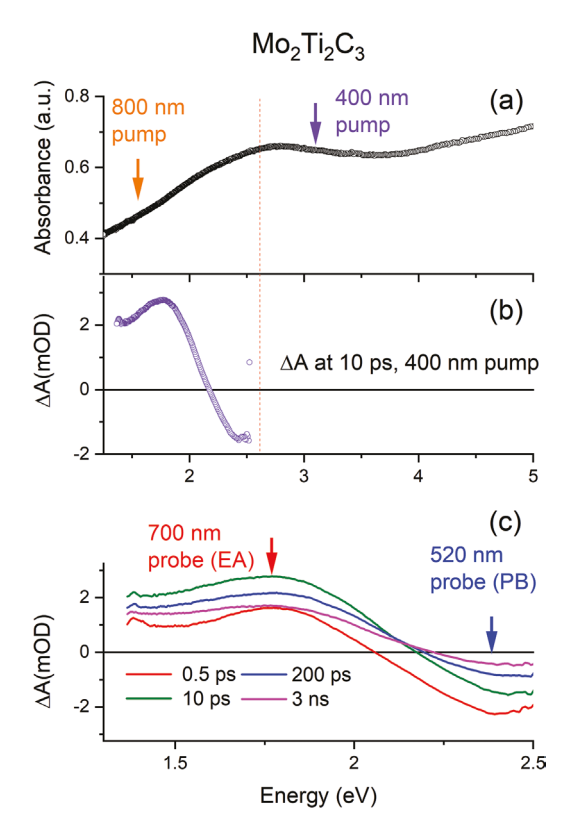


**Figure 2.**  $Mo_2Ti_2C_3$ . a) UV–vis absorbance. Dashed line indicates presumed plasmon. b) Transient absorbance 10 ps after excitation with 400 nm pulse. c) Transient absorbance at four different times indicated on plot after excitation.

vertical line). Transient changes in the optical absorption after a 400 nm excitation (Figure 2b,c) are qualitatively identical to those seen in  $\text{Ti}_3\text{C}_2$ ; absorption is suppressed at the position of the extinction peak seen in static absorption. We also observe an enhanced absorption band centered at  $\approx$ 700 nm, or 1.77 eV (EA). Again, both features persist for times > 3 ns without appreciable spectra shifts.

The respective results for Nb<sub>2</sub>C are shown in Figure 3. While the intrinsic free carrier concentration in this MXene has not yet been reported, it is presumed to be orders of magnitude lower than in Ti<sub>3</sub>C<sub>2</sub> and even in Mo<sub>2</sub>Ti<sub>2</sub>C<sub>3</sub>. Maleski at el. reported a broadband near-IR absorbance centered at 915 nm (1.35 eV) in Nb<sub>2</sub>C films. In our film, Vis-NIR absorption is quite low. However, we do observe a peak centered at ≈730 nm or 1.7 eV (see vertical dashed line in Fig. 3a, b) superimposed on a broad background, which can be seen when the experimental spectrum is scaled to enhance the VIS-NIR range (Figure 3a). The lower intensity of this peak might indeed be due to a much lower, but still finite, carrier density in Nb<sub>2</sub>C compared with the two other MXenes. Similar to the other two films, photoexcitation results in an absorption bleach centered at the weak absorption peak seen in the static spectrum (Figure 3b), which leads us to conclude that it, too, is an LSPR. Like in the case of the other two films, we label bleaching of absorption at the energy of the presumed LSPR as PB feature (Figure 3c). The latter feature is prominent at early times after photoexcitation, but decays significantly faster than the in other two materials

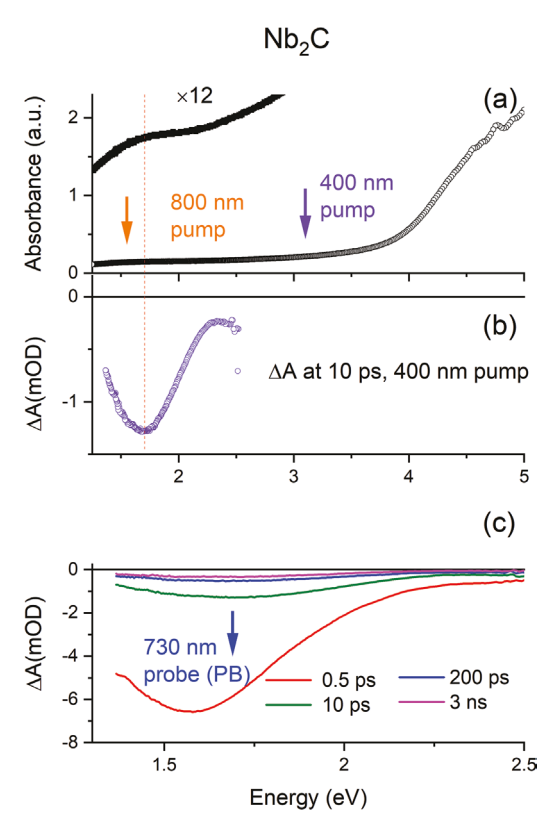


**Figure 3.** Nb<sub>2</sub>C. a) UV–vis absorbance. Dashed line indicates energy of presumed plasmon. Top curve is experimental data multiplied by 12 for clarity. b) TA 10 ps after excitation with 400 nm pulse. c) TA at four different times, indicated on panel, after excitation.

and almost disappears by 200 ps (Figure 3c). Unlike  $Ti_3C_2$  and  $Mo_2Ti_2C_3$ , the TA spectra of  $Nb_2C$  do not have EA features in our experimental spectral range.

Figure 4 compares TA spectra taken 10 ps after excitation with 400 nm and 800 nm light in all three MXenes. The two excitation wavelengths are shown by arrows in Figures 1a, 2a, and 3a. In all cases, two different excitation wavelengths fall on different sides of our presumed LSPR absorption peak. While the absolute magnitude of the TA is somewhat weaker for the 800 nm excitation due to a lower pump absorption, qualitatively, the spectral shapes are identical and insensitive to excitation wavelengths. The independence of the observed features -PB and EA – on the excitation photon energy can be seen in the normalized kinetics recorded at the characteristic probe wavelength (742 nm for PB and 520 nm for EA for Ti<sub>3</sub>C<sub>2</sub>, 520 nm for PB and 700 nm for ESA for Mo<sub>2</sub>Ti<sub>2</sub>C<sub>3</sub>, and finally 730 nm for PB in Nb<sub>2</sub>C), shown in Figure 5 (a,b,d,e,g). In all three films, temporal evolution of PB and EA is independent not only of the excitation wavelengths but also of the excitation fluences in the range studied.

The next question to consider is: How does photoexcitation impact free carrier conductivity? To answer this question, we used TRTS with the same excitation wavelengths of 800 and 400 nm as used for TA. The THz probe has a 1–8 meV bandwidth and is thus sensitive to low energy excitations such as free carrier absorption. In fact, negative changes in peak THz probe transmissions can be used to monitor photoinduced

www.advmat.de

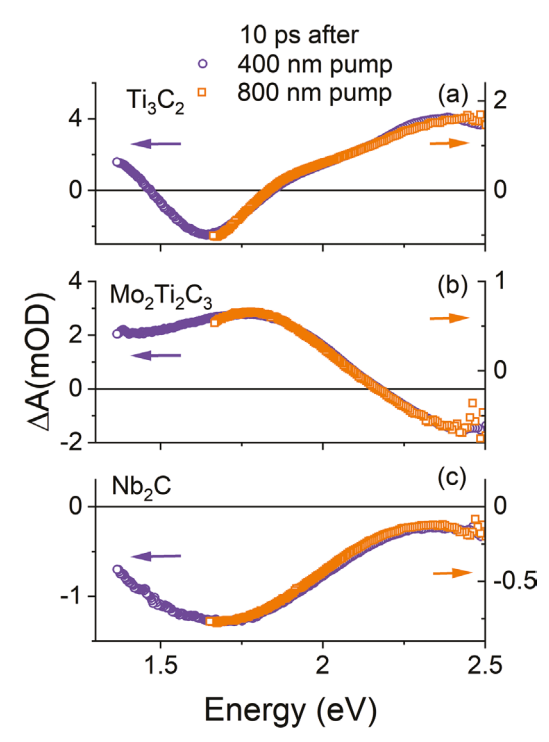


**Figure 4.** TA 10 ps after excitation with 400 nm (purple symbols, left scale) and 800 nm (orange symbols, right scale) in, a)  $Ti_3C_2$ , b)  $Mo_2Ti_2C_3$ , and c)  $Nb_2C$ .

transient conductivity.[33] Normalized TRTS traces for all three films are shown in Figure 5 (c,f,h). All observed photoexcited TA and TRTS transients can be fit by multiple exponentials, with decay times summarized in Table 1. In this table, we defined several timescales:  $t_0$  - in the 0.1 to 8 ps range - for the fastest relaxation processes, that typically corresponds to carrier-carrier scattering as well as to fast carrier trapping. The second set,  $t_1$  and  $t_2$  in the intermediate time range - from 9 ps to 1000 ps -correspond to photoexcited carrier trapping at various defect states and flake edges, as well as, possibly, due to lattice cooling. The final times -  $t_3 > 3$  ns - covering long time scales that are outside of our experimental window and appear as a near-constant offset are attributed almost exclusively to thermal effects. In addition, EA in Mo2Ti2C3 shows a rise that is slower than the others, which is limited by our experimental time resolution (0.05 ps for TA and 0.4 ps for TRTS); the rise time fits well to a two-exponential rise function, and the corresponding times are also listed in Table 1.

### 3. Discussion

Transient absorption features - observed at 742 nm in  $Ti_3C_2$ , at 520 nm in  $Mo_2Ti_2C_3$ , and at 730 nm in  $Nb_2C$  - have the same qualitative ultrafast transient optical properties. Specifically, regardless of the photon energy (1.55 eV vs 3.1 eV), or whether the excitation is near-resonant, or off-resonant with respect to the static absorption peak as in the case of  $Ti_3C_2$  and  $Nb_2C$ , optical excitation results in a sustained absorption decrease centered at the same energy as absorption peaks observed in

static UV-vis spectroscopy. We also do not observe any qualitative changes to the TA spectra in response to a nearly two-fold change in excitation fluence. We, therefore, ascribe the negative peak in TA spectra in all three MXenes to transient optically-induced broadening (damping) of the LSPR peak and conclude that the LSPR features govern visible-near-IR optical response in these materials.

The transient bleach of plasmon modes has been widely studied in both bulk, and nanoscale, metals. [28,29,34-38] It results from optical excitations of the free electron distribution and the creation of a non-equilibrium hot carrier distribution over sub-100 fs time scales as a result of electron-electron interactions.<sup>[28]</sup> As the hot carrier distribution relaxes by electron-phonon interactions, it transfers its energy to the crystal lattice over times scales ranging from sub-ps to several ps, which in turn eventually cools by transferring thermal energy to the surroundings, viz. thermal diffusion and/or radiation. [29,34,39] These processes result in plasmon bleach recovery. The time scale of this relaxation is determined by the electron-phonon coupling strength and by the thermal conductivities of individual nanostructures and their ensembles or films, which determine how fast the excess heat dissipates. In conventional Au or Ag plasmonic metallic nanostructures, recovery of the plasmon bleach time ranges from picoseconds to tens of picoseconds.[30] It is known to be slower in transition metals like Mo, Cr, or Ru, [39] as well as in metallic binary nitrides such as TiN and ZrN, where lattice cooling occurs over hundreds of picoseconds.[40] In those materials, studies have revealed a strong electron-phonon coupling, 25–100 times greater than in Au, which leads to thermalization of photoexcited electrons with the crystal lattice on a sub-100 fs and greater lattice heating than observed for noble metals under comparable conditions.

Here, we observe PB relaxation that is considerably slower than in noble metals and even the refractory binary nitrides, TiN and ZnN. In fact, in Ti<sub>3</sub>C<sub>2</sub>, initial fast sub-ps relaxation is followed by ≈110 ps decay, and then the PB decays over ns time scales, with ≈50% of the observed bleach remaining at 2.5–3 ns (Figures 1 and 5a). In Mo<sub>2</sub>Ti<sub>2</sub>C<sub>3</sub>, initial rapid decay, over sub-ps and 9 ps time scales, likely corresponds to carrier-carrier and carrier-phonon relaxation, is followed by a significantly slower, ≈600 ps relaxation and a small, but non-zero, longer (> 3 ns), decay, that we ascribe to energy dissipation to the environment. Finally, in Nb2C, because film conductivities are below the measurable threshold not only for hand-held multimeters but also in the THz time-domain spectroscopy (Figure S2, Supporting Information) we assume the intrinsic free carrier density is quite low. It is non-zero, however, as evidenced by a weak but observable plasmon absorption peak in the static UV-IR spectrum (Figure 3a). Photoexcitation injects new hot charge carriers, resulting in a quite broad PB feature that initially recovers over sub-ps and 4 ps time scales as photoexcited carriers thermalize by carrier-carrier and carrier-lattice scattering. Final recovery proceeds over a ≈90 ps time scale, significantly faster than in the other two MXenes but still slower than in noble metal nanoparticles.

What is known about the thermal properties of MXenes that might shed additional light on these long thermal relaxation time scales? Reported experimental room temperature thermal conductivity of  $2.84~W~m^{-1}~K^{-1}$  for a  $Ti_3C_2$  film is orders

15214095, 2023, 8, Downloaded from https://onlinelibrary.wiley.com/doi/10.1002/adma.202208659 by Worcester Polytechnic Institut, Wiley Online Library on [01/08/2023]. See the Terms and Conditions (https://onlinelibrary.wiley.com/term

and-conditions) on Wiley Online Library for rules of use; OA articles are governed by the applicable Creative Commons License

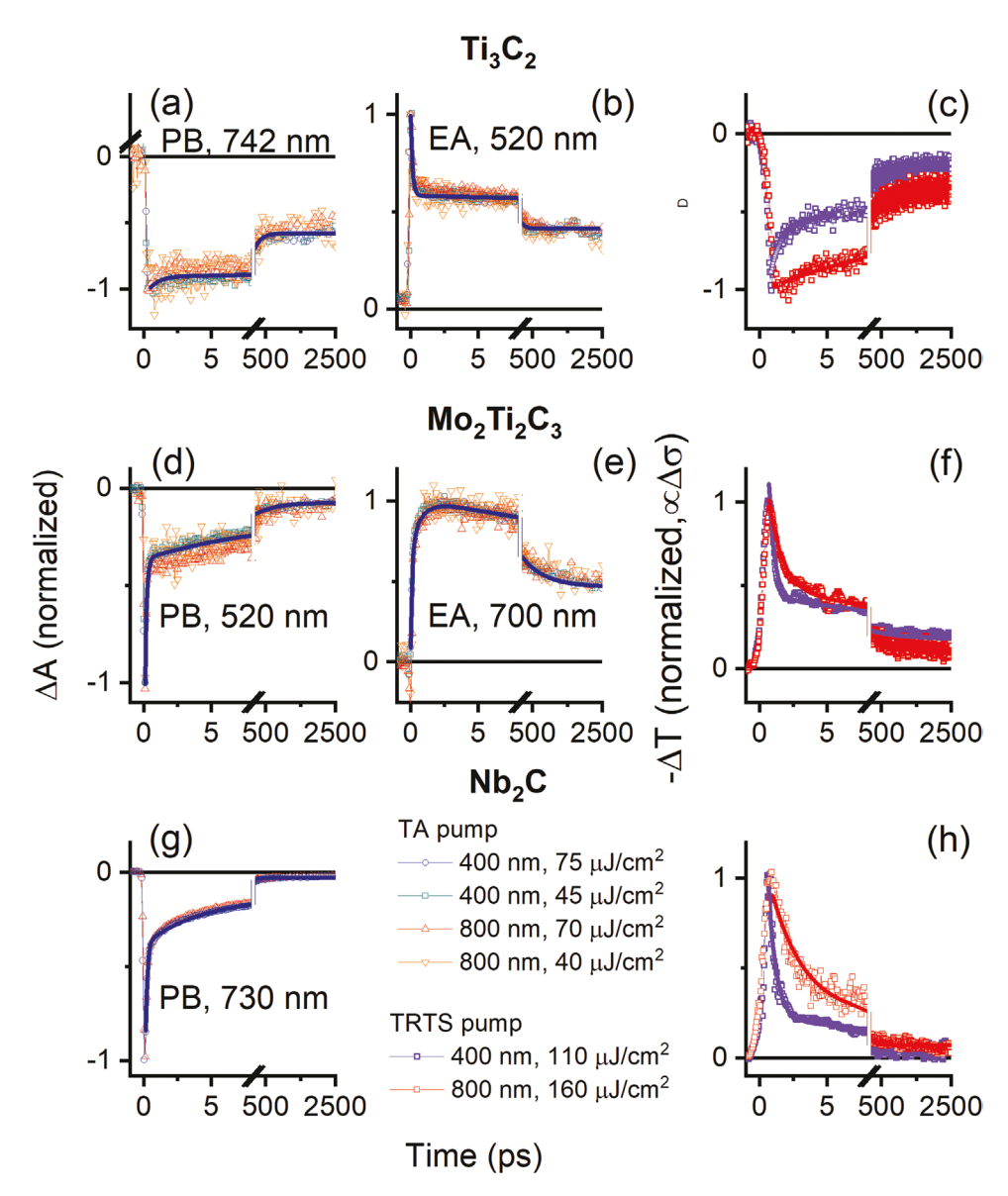


Figure 5. TA and TRTS kinetic for Ti<sub>3</sub>C<sub>2</sub> (a,b,c), Mo<sub>2</sub>Ti<sub>2</sub>C<sub>3</sub> (d,e,f)), and Nb<sub>2</sub>C (g,h). Normalized TA kinetic traces are shown in (a,b,d,e,g), and TRTS decays in (c,f,h). Pump wavelength and fluence values shown in the legend, and TA probe wavelengths are indicated in each panel.

of magnitude lower than that for conventional metals such as gold or copper.[41,42] The Wiedemann-Franz law analysis relating experimental electrical and thermal conductivity values for a Ti<sub>3</sub>C<sub>2</sub> film also yields a surprising result that electronic contribution to the measured thermal conductivity is only ≈2–3%.[43] In agreement with this observation, Gholivand et al. used DFT, and the phonon Boltzmann transport equation, to predict that low frequency (<400 cm<sup>-1</sup>) phonons are responsible for most of the heat transport. They also conclude that the lattice thermal lattice conductivity is strongly dependent on surface terminations, ranging from 108 W m<sup>-1</sup> K<sup>-1</sup> in fluorine-terminated Ti<sub>3</sub>C<sub>2</sub> to 11 W m<sup>-1</sup> K<sup>-1</sup> in its oxygen-terminated counterpart.<sup>[42]</sup> These results are comparable to calculations of thermal conductivity in F- and O-terminated Ti<sub>2</sub>C.<sup>[44]</sup> In Nb<sub>2</sub>C, Huang et al. predict that electron-phonon scattering is nearly as strong as phononphonon scattering. The latter is typically what determines

thermal conductivity in most materials. The unusually large electron-phonon scattering results in large reductions in lattice thermal conductivity.[31] Indeed, it is likely that the same mechanism is at play in Ti<sub>3</sub>C<sub>2</sub> and other MXenes, significantly limiting the intrinsic (intra-flake) thermal conductivity. Unusually strong electron-phonon scattering may also be behind the high photothermal conversion efficiency reported for both Nb<sub>2</sub>C and Ti<sub>3</sub>C<sub>2</sub> [26,27] Hot phonon bottlenecks, a phenomenon where the rapidly created and long-lived hot phonon population blocks further phonon emission and impedes carrier cooling, has been recently proposed as a mechanism behind the remarkably long hot carrier lifetime in 2D perovskites.<sup>[45,46]</sup> This effect may also be at play in MXenes and thus warrants further theoretical and experimental investigations. Finally, it is reasonable to assume that the long-range thermal conductivity of MXene films, responsible for carrying away heat over length



www.advmat.de

Table 1. TA and TRTS: decay times resulting from fitting kinetics shown in Figure 5 to multi-exponential decay times. In addition, rise time is given for the  $Mo_2Ti_2C_3$  EA.

MXene	TA: Plasmon Bleach	TA: Excited State Absorption	TRTS: 400 nm excitation	TRTS: 800 nm excitation
Ti <sub>3</sub> C <sub>2</sub>	Probe 742 nm	Probe 520 nm	$t_0 = 0.7 \pm 0.1 \text{ ps}$	$t_0 = 7.0 \pm 0.5 \text{ ps}$
	$t_0 = 0.7 \pm 0.1 \text{ ps}$	$t_0 = 0.4 \pm 0.1 \text{ ps}$	$t_1 = 11 \pm 1 \text{ ps}$	$t_1 = 130 \pm 20 \text{ ps}$
	<i>t</i> <sub>1</sub> N/A	<i>t</i> <sub>1</sub> N/A	$t_2 = 410 \pm 20 \text{ ps}$	$t_2 = 920 \pm 100 \text{ ps}$
	$t_2 = 190 \pm 10 \text{ ps}$	$t_2 = 110 \pm 10 \text{ ps}$	$t_3 > 3$ ns	$t_3 > 3 \text{ ns}$
	$t_3 > 3$ ns	$t_3 > 3$ ns		
$Mo_2Ti_2C_3$	Probe 520 nm	Probe 700 nm	$t_0 = 0.4 \pm 0.1 \text{ ps}$	$t_0 = 1.1 \pm 0.1 \text{ ps}$
	$t_0 = 0.12 \pm 0.01 \text{ ps}$	Rise: $t_{1r} = 0.12 \pm 0.02 \text{ ps}$	$t_1 = 14 \pm 1 \text{ ps}$	$t_1 = 16 \pm 1 \text{ ps}$
	$t_1 = 9 \pm 1 \text{ ps}$	$t_{2r} = 0.8 \pm 0.1 \text{ ps}$	$t_2 = 970 \pm 100 \text{ ps}$	$t_2 = 800 \pm 100 \text{ ps}$
	$t_2 = 610 \pm 100 \text{ ps}$	Decay:	$t_3 > 3$ ns	$t_3 > 3 \text{ ns}$
	$t_3 > 3$ ns	t <sub>0</sub> N/A		
		$t_1 = 15 \pm 2 \text{ ps}$		
		$t_2 = 650 \pm 50 \text{ ps}$		
		$t_3 > 3$ ns		
Nb₂C	Probe 730 nm	N/A	$t_0 = 0.6 \pm 0.1 \text{ ps}$	$t_0 = 1.51 \pm 0.1 \text{ ps}$
	$t_0 = 0.12 \pm 0.01 \text{ ps}$		$t_1 = 13 \pm 1 \text{ ps}$	$t_1 = 14 \pm 1 \text{ ps}$
	$t_1 = 4.0 \pm 0.2 \text{ ps}$		$t_2 = 300 \pm 30 \text{ ps}$	$t_2 = 300 \pm 30 \text{ ps}$
	$t_2 = 90 \pm 10 \text{ ps}$		t <sub>3</sub> N/A	t <sub>3</sub> N/A
	t <sub>3</sub> N/A			

scales larger than the average lateral dimensions of a single flake, is further limited by the thermal resistance between the stacked flakes.<sup>[41]</sup> Like electrical conductivity, thermal conductivity of MXene films is thus critically dependent on chemical terminations,<sup>[42]</sup> presence of flake edges and intercalated species between the flakes, and thus, ultimately, on film preparation, density and thickness.

The observed unusually slow recovery of plasmon damping in MXene films following optical excitation suggests high carrier-phonon scattering that allows rapid and efficient localized heating of the crystal lattice and limits thermal conductivity, as low-frequency acoustic phonons are strongly scattered not only off each other, flake edges and defects but also by free carriers. We note here that PB recovery is the slowest in the MXene with the highest carrier density, Ti<sub>3</sub>C<sub>2</sub>, and the fastest in Nb<sub>2</sub>C.

To get additional insight, we examined the influence of photoexcitation on free carrier dynamics using TRTS. We have earlier reported on the THz studies of intrinsic and photoinduced conductivity in Ti<sub>3</sub>C<sub>2</sub> and in Mo<sub>2</sub>Ti<sub>2</sub>C<sub>3</sub>.<sup>[7,8,47]</sup> A recent study by Zheng et al. examined THz photoconductivity in Ti<sub>3</sub>C<sub>2</sub> and Nb<sub>4</sub>C<sub>3</sub>, the latter a Nb-based material with properties similar to Nb<sub>2</sub>C.<sup>[48]</sup> Here, our observed THz TDS and TRTS dynamics agree with previous reports. We find that Ti<sub>3</sub>C<sub>2</sub> films have high static THz conductivities,  $\approx 3500 \ (\Omega \ cm)^{-1}$  (Figure S1, Supporting Information). As in previous studies, photoexcitation of metallic Ti<sub>3</sub>C<sub>2</sub>, with either 400 or 800 nm pulses, results in a transient reduction of THz conductivity as indicated by  $-\Delta T < 0$ , are presumed to occur due to increased carrier scattering.[7,47,48] Like in our earlier report, we find that the recovery time is remarkably slow, with as much as ≈ 30% of the peak signal persisting for ≈3 ns and longer. The slowest relaxation component for recovery of conductivity suppression can be ascribed to slow cooling of the crystal lattice; the same mechanism responsible for the slowest component of PB recovery. In our previous study, we initially cast doubts on the thermal origin of long-lived optical conductivity suppression in Ti<sub>3</sub>C<sub>2</sub>

that persists for several orders of magnitude longer than in conventional methods, because we found recovery dynamics to be temperature-independent from 90 K to 300 K.[7] In conventional materials, lattice thermal conductivity is determined primarily by phonon-phonon scattering that is typically temperature-dependent. However, a recent study by Huang et al., already noted above, uncovered the dominant role played by scattering of acoustic phonons on free carriers in determining the thermal conductivity of Nb<sub>2</sub>C (and likely other MXenes as well).[31] In that study, they found that such electron-phonon scattering is nearly temperature-independent. In light of this discovery, it is reasonable to assert that slow recovery of both the PB feature and optically induced conductivity suppression in Ti<sub>3</sub>C<sub>2</sub> is a consequence of its ultra-low thermal conductivity, which in turn stems from a significant and temperature-insensitive scattering of low-frequency acoustic phonons on a large number of free carriers.

Turning to earlier times (sub-1000 ps) dynamics in photoexcited  ${\rm Ti}_3{\rm C}_2$ , we find that TRTS dynamics, unlike PB recovery dynamics, depend on excitation photon energy (Figure 5c,f,h). At early times after excitation, we find that 400 nm excitation results in a fast (instrument-limited,  $\approx 0.4$  ps) decrease in conductivity, followed by a fast,  $\approx 1$  ps initial recovery. For the 800 nm excitation, the fastest, 1 ps, recovery component is not observed. With both excitation photon energies, inter-band excitations of new electron-hole pairs is possible in addition to intra-band excitation of hot electrons. We hypothesize that higher photon energy results in more inter-band excitations of carriers deep in the valence and conduction bands, resulting in faster initial carrier-carrier scattering and trapping.

Plasmon bleach recovery, on the other hand, has the same kinetics for both 400 and 800 nm excitations even at early times, as it occurs because of a dramatically increased electron gas temperatures, followed by a rapid increase in the lattice temperature, and concomitant enhanced carrier-carrier and carrier-lattice scattering. We also note that enhanced

ADVANCED MATERIALS

www.advmat.de

absorption (EA) in TA spectroscopy of Ti<sub>3</sub>C<sub>2</sub>, following the initial sub-ps rapid relaxation, follows similar kinetics as the PB feature, indicating that it, too, results from strong broadening of the plasmon absorption peak following photoexcitation. The exact values of recovery decay times  $t_0$ ,  $t_1$  and  $t_2$  depend on film preparation as they are likely sensitive to the presence of defects, intercalants, and to specific surface terminations.<sup>[18]</sup> As noted earlier, we hypothesize that the fastest, sub-ps to few-ps decay times represent carrier-carrier scattering, while the slower time scales correspond to phonon scattering, trapping and recombination of photoexcited carriers and slow heat dissipation to the environment over the nanoseconds time scales. Future experiments where the surface terminations, intercalants, as well as morphology of individual flakes can be varied in a controlled manner will need to be carried out to ascribe those observed decay times scales to specific relaxation processes, carrier trapping and/or recombination mechanisms.

In the case of Nb<sub>2</sub>C, DFT calculations find that bare as well as O- and OH-terminated flakes are metallic,[31,49] while nitrogen terminations opens a narrow band gap of  $\approx 60$  meV.<sup>[50]</sup> XPS results (Figure S1 and Table S2, Supporting Information) show a mix of O and OH terminations in our Nb<sub>2</sub>C film. At the same time, we find that static THz conductivity of Nb<sub>2</sub>C is negligible (Figure S2, Supporting Information), and photoexcitation results in a positive photoconductivity (Figure 5h), similar to the reported behavior of another Nb-based MXene, Nb<sub>4</sub>C<sub>3</sub>.<sup>[48]</sup> Previous temperature-dependent electronic measurements showed that conductivity of Nb<sub>2</sub>C is several orders of magnitude lower compared to Ti<sub>3</sub>C<sub>2</sub>, and that it decreases further at low temperatures, viz. inconsistent with behavior of traditional bulk metals.<sup>[51]</sup> Halim et al. suggested that charge carriers may be localized within the individual flakes, and the longrange transport is limited by variable range hopping. [51] Taken together, these observations suggest that Nb<sub>2</sub>C is semi-metallic, with low static free carrier density and a strong localization of the existing carriers hindering their long-range transport.

We find that after an initial fast rise, transient photoinduced conductivity relaxation can be well described by a three-exponential decay (Table 1). The fast component -  $\approx 0.6$  ps for 400 nm excitation and ≈ 1.5 ps for 800 nm, excitation - is likely is in the carrier-carrier scattering timescales. In addition, in their study of Nb<sub>4</sub>C<sub>3</sub>, Zhang et al. ascribed this fast relaxation to rapid trapping of inter-band excited carriers on defect states as its contribution increased in films that were more oxidized.[48] The initial fast relaxation is followed by a slower decay occurring in the 12-13 ps time scales, and finally the relaxation to nearly background levels over ≈300 ps time scales, irrespective of the excitation wavelength (Figure 5h). Comparing these dynamics to PB recovery, we find that it, too, nearly fully recovers within 300 ps. Unlike Ti<sub>3</sub>C<sub>2</sub>, which has high equilibrium free carrier density, most of free carriers near the Fermi edge in Nb<sub>2</sub>C are photoexcited. If those carriers indeed inhibit rapid heat dissipation, then as these optically injected carriers are trapped, or recombined, the lattice cooling by efficient phonon transport

The third MXene we studied,  $Mo_2Ti_2C_3$ , combines the properties of the other two. It has over an order of magnitude lower conductivity compared to  $Ti_3C_2$ ,  $\approx 160~(\Omega~cm)^{-1}$  (Figure S1, Supporting Information), in good agreement with our previous

THz spectroscopic study of this material. [8] DFT modeling predicts its metallicity,[52] and its long-range transport is limited by the variable range hopping between flakes, similar to granular metals.<sup>[53]</sup> The observed positive transient photoconductivity indicates that the inter-band excitation of the additional charge carriers dominates over intra-band excitation of intrinsic carriers. Moreover, our earlier TRTS study of frequency-resolved Mo<sub>2</sub>Ti<sub>2</sub>C<sub>3</sub> photoconductivity revealed that additional photoexcited free carriers exhibit higher carrier mobility within the flakes, as represented by the carrier scattering times of ≈20 fs for intrinsic carriers, versus ≈50-70 fs for photoexcited carriers, and enhanced inter-flake transport, represented by the Drude-Smith c parameter, a phenomenological measure of carrier localization over the probed length scales. We reported  $c = -0.941 \pm 0.007$  (highly localized) for intrinsic carriers, and  $c = -0.67 \pm 0.02$  (less localized) for photoexcited carriers, which can be explained by an excitation-induced heating enhancing inter-flake carrier hopping.<sup>[8]</sup> We find that photoconductivity recovery in Mo<sub>2</sub>Ti<sub>2</sub>C<sub>3</sub> is qualitatively similar to Nb<sub>2</sub>C, with a fast component (0.4 ps for 400 nm and 1.1 ps for 800 nm excitation) followed by slower components. The fastest component, which we again ascribe to carrier trapping, is somewhat less prominent in Mo<sub>2</sub>Ti<sub>2</sub>C<sub>3</sub>, possibly owing to a larger thickness of individual flakes in this M<sub>4</sub>C<sub>3</sub>-type MXene. Slower components have time scales of 14–16 ps and 800–1000 ps, with a small, but evident, contribution of a longer, >3 ns, thermal dissipation component, similar to Ti<sub>3</sub>C<sub>2</sub>.

Correlating TRTS and TA dynamics in  $Mo_2Ti_2C_3$ , we find that PB recovery proceeds over times scales that are comparable to the relaxation of its photoinduced conductivity. The presence of a long, >3 ns, component in PB relaxation, albeit much weaker compared to  $Ti_3C_2$ , can be attributed to the presence of a significant equilibrium-free carrier density that, as discussed earlier, suppresses thermal relaxation.

Unlike Ti<sub>3</sub>C<sub>2</sub>, we observe an interesting feature in the enhanced absorption that is centered in the red portion of the spectrum (≈700 nm) for Mo<sub>2</sub>Ti<sub>2</sub>C<sub>3</sub> (Figures 2b,c, 4b, and 5e). We know that at least in part, the origin of the EA in the vicinity of PB is still due to plasmon band damping and changed dielectric function due to increased lattice temperature. In addition, it is possible to encounter photoinduced absorption by the carriers that are promoted to the excited states in the band structure or trapped in the defect states. In the case of Mo<sub>2</sub>Ti<sub>2</sub>C<sub>3</sub>, the buildup of ESA is slower than in Ti<sub>3</sub>C<sub>2</sub> and proceeds on a time scale commensurate with the initial recovery of the PB feature. We posit therefore that at early times, some of the photoexcited carriers indeed become trapped, or scatter into the excited states that give rise to additional ESA superimposed on the usual plasmon broadening "wing" effect. The nature of these states will have to be investigated in future studies, and varying the Mo-Ti ratio (e.g., Mo<sub>2</sub>Ti<sub>2</sub>C<sub>3</sub> vs Mo<sub>2</sub>TiC<sub>2</sub>) as well as exploring the role, if any, of defects and intercalated species, in ESA. These should be some of the first steps toward fully uncovering the nature of the observed effect.

## 4. Summary

We have, for the first time, applied two complementary ultrafast spectroscopic tools, TA and TRTS, to uncover the nature



www.advmat.de

of photoexcitations and investigate their dynamics in three different MXenes: Ti<sub>3</sub>C<sub>2</sub> Mo<sub>2</sub>Ti<sub>2</sub>C<sub>3</sub> and Nb<sub>2</sub>C. We discovered that all three exhibit plasmonic properties in the visible and near-IR spectral range. Photoexcitation with either near-IR pulses (800 nm, or 1.55 eV) or ultraviolet, UV, pulses at 400 nm (3.1 eV) results in rapid heating of the crystal lattice, as evidenced by the significant broadening of the plasmon mode and concomitant plasmon bleach in transient optical absorption. Monitoring plasmon bleach recovery kinetics provided new insights into thermal properties in MXenes and revealed uncharacteristically slow heat dissipation compared to other plasmonic materials such as noble metal nanoparticles. We ascribe this slow recovery to a low thermal conductivity in all three MXenes. As previous theoretical studies posit, lattice thermal conductivity is a dominant contribution to the heat diffusion in MXenes, and low thermal conductivity stems from scattering of low-energy phonons by free charge carriers.<sup>[31]</sup> We observe the slowest lattice cooling, proceeding over nanoseconds, in MXene with the highest equilibrium free carrier density (≈10<sup>22</sup> cm<sup>-3</sup>), Ti<sub>3</sub>C<sub>2</sub>, and the fastest, over ≈100 ps, in Nb<sub>2</sub>C, where the free carriers that presumably limit thermal diffusion, are almost exclusively optically injected. providing evidence of the unprecedently low lattice thermal conductivity in MXenes. Strong electron-phonon scattering responsible for unusually low thermal conductivity is in agreement with the highly efficient photothermal conversion efficiency in MXenes demonstrated in several recent studies. [26,27] Finally, we resolved the outstanding question about the mechanism behind the long-lived suppression of conductivity and enhanced transmission of THz radiation due to the photoexcitation in Ti<sub>3</sub>C<sub>2</sub>,<sup>[7,47]</sup> and ascribe it to the slow thermal relaxation. These findings elucidate the nature of optical excitations in MXenes with different chemistries and free carrier densities, and provide new insights into their unique thermal properties, and lay the foundations for their application in solar energy conversion and other photonic applications.

#### 5. Experimental Section

MAX Phase Preparation: Ti<sub>3</sub>AlC<sub>2</sub>, (Ti<sub>3</sub>C<sub>2</sub> precursor) was synthesized by heating a ball-mixed mixture of TiC, Al, and Ti (Alfa Aesar, 99.5% purity) powders in a molar ratio of 2:1.05:1, respectively, under flowing argon (Ar) at a rate of 5 °C min $^{-1}$  to 1350 °C and a holding time of 2 h. The resulting solid is milled and sieved (–400 mesh) to obtain a powder with particle size of <38  $\mu m$ .

Nb<sub>2</sub>AlC, (Nb<sub>2</sub>C precursor) was synthesized by heating a ball-mixed mixture of Nb (Alfa Aesar, 99.8% purity), Al (–325 mesh, Alfa Aesar, 99.5% purity, ≤44 μm), and C (–300 mesh, Alfa Aesar, 99%, ≤48 μm) powders with a molar ratio of 2:1.1:1, respectively. Excess aluminum compensated for evaporation and the aluminothermic reduction of native metal oxides. Powders were mixed in a polyethylene jar with zirconia milling balls for ≈ 9 h. The mixed powders were cold pressed using a 25.4 mm diameter steel die using a load corresponding to 200 MPa pressure. The cold-pressed puck was placed in an alumina boat and sintered in a tube furnace under argon, Ar, atmosphere at 1600 °C for 4 h with a heating rate of 3 °C min<sup>-1</sup>. The resulting solid was then drilled into powder and sieved through a –400 mesh to obtain a powder with particle size of <38 μm.

 $Mo_2Ti_2AlC_3$ , ( $Mo_2Ti_2C_3$  precursor) was synthesized by ball milling Mo, Ti, Al, and C powders (all from Alfa Aesar, 99.5% purity), with mesh sizes of -250, -325, -325, and -300, respectively, for 18 h using zirconia balls in polyethylene bottles, in a molar ratio of 2:2:1.3:2.7, respectively.

The powder mixture was then heated in a covered alumina crucible at 5  $^{\circ}$ C min<sup>-1</sup> to 1600  $^{\circ}$ C and held for 4 h under flowing Ar. After cooling, the porous compact was drilled and milled, then sieved through a –400 mesh to obtain a powder with particle size of <38  $\mu$ m.

MXene Synthesis:  $Ti_3C_2$ : The  $Ti_3AlC_2$  powders were used for preparing the colloidal suspension of MXene. One gram of lithium fluoride (LiF) was dissolved in 10 mL of 12 m HCl, followed by the slow addition of the powders. The solution was magnetically stirred on a hot plate at 35 °C for 24 h. The powder was then washed seven times with distilled water in a centrifugation and decantation process (3500 rpm, 2 min) until the supernatant reached a pH of  $\approx$  6 and spontaneous delamination was observed. 20 mL of distilled water was then added to the sediment and the mixture was sonicated for 1 h at room temperature under bubbling Ar, and subsequently centrifuged at 3500 rpm for 1 h. The supernatant collected contained mostly single  $Ti_3C_2T_7$  flakes.

Nb₂C: The colloidal suspension containing mostly single flakes of Nb₂C was obtained through etching of 1 g Nb₂AlC powder in 10 ml of 50% HF solution while gain magnetically stirring for 72 h at 55 °C. After the etching process, the superfluous HF was removed by a repeated washing process with DI water, in a centrifugation and decantation process, until the pH of the supernatant reached  $\approx \!\! 7$ . The multilayered MXene sediment from the washing process was then dispersed in 2 ml of 25% tetrabutyl-ammonium hydroxide (TBAOH). The mixture was washed with 200 proof ethanol solution twice, followed by a final DI water washing process. After sonication of the suspension for 1 h, and its centrifugation for an hour, the supernatant was comprised of a colloidal suspension containing mostly single to few flakes of Nb₂C.

 $Mo_2Ti_2C3$ : The colloidal suspension containing mostly single flakes of  $Mo_2Ti_2C_3$  was obtained through etching of 1 g  $Mo_2Ti_2AlC_3$  powder in 10 ml of 50% HF solution while magnetically stirring for 72 h at 55 °C. After the etching process, the superfluous HF was removed by repeated washing process with DI water, in a centrifugation and decantation process, until pH of the supernatant reached  $\approx$ 7. The multilayered MXene sediment from the washing process was then dispersed in 2 mL of 25% TBAOH. The mixture was washed with 200 proof ethanol solution twice, followed by a final DI water washing process. After sonication of the mixture for 1 h, and its centrifugation for an hour, the supernatant, comprised of colloidal suspension containing single flakes of  $Mo_2Ti_2C_3$  MXene, was collected.

X-Ray Photoelectron Spectroscopy (XPS): A K-Alpha X-ray Photoelectron Spectrometer (XPS) System from Thermo Fisher Scientific was utilized to collect XPS spectra in a constant analyzer energy mode. Survey spectra were collected from -10 eV to 1350 eV with the flood gun on, averaged over five scans with a step size of 1.0 eV, a 10 ms dwell time, a pass energy of 200 eV, and a 400  $\mu m$  X-ray spot size. High-resolution spectra were collected according to the atomic standard range listed in Avantage 5.9917 software for each element with the flood gun on, averaged over five scans with a step size of 0.05 eV, a 300 ms dwell time, a pass energy of 50 eV and a 400  $\mu m$  X-ray spot size. Peaks in the spectra were assigned and atomic percentages were calculated using CasaXPS software. For each sample investigated, the spectra were collected from three distinct areas and the average atomic percentage of each element was calculated across the three areas. An element was determined to be present when the average atomic percentage was at least 0.1%.

*UV-vis Spectroscopy*: A UV-vis spectrometer (Evolution 300, Thermo Fisher Scientific, Waltham, MA) was used to collect UV-vis spectra of the MXene films in transmission mode.

Transient Absorption (TA) Spectroscopy: The TA measurements were carried out using a HARPIA-TA Ultrafast Transient Absorption Spectrometer (Light Conversion). In the measurement, 1030 nm, 290 fs pulses from a Carbide (Light Conversion) laser generated probe white light through a sapphire crystal. An optical parametric amplifier (Orpheus, Light Conversion) generated 400 and 800 nm pump pulses. Pump-induced differences in absorption were detected in transmission mode by an Andor spectrograph and a Si photodiode array as a function of pump-probe delay time.

Time-Resolved THz Spectroscopy: The THz spectroscopy measurements were carried out as described previously, for example, in Ref. [47] In brief,



www.advmat.de

ps-long THz pulses with a bandwidth between 0.25–2.2 THz (1–9 meV) were generated by optical rectification of 100 fs, 800 nm pulses from a regeneratively-amplified laser (Coherent Libra) in a 1 mm thick [110] ZnTe crystal. The pulse was focused onto the sample using off-axis parabolic mirrors, and transmitted THz pulses were detected using free-space electro-optic sampling in a second 1 mm thick [110] ZnTe crystal. In THz TDS, coherent detection of the amplitude and phase of THz probe pulses in the time domain allowed for the extraction of a sample's frequency-dependent complex conductivity by analyzing the amplitudes and phases of the THz pulses transmitted through the substrate alone and the sample on the substrate. [33] In TRTS, films were photoexcited by 800 or 400 nm, 100 fs pulses. Photoinduced changes in the complex THz conductivity were probed using a time-delayed THz pulse.

### **Supporting Information**

Supporting Information is available from the Wiley Online Library or from the author.

#### **Acknowledgements**

Approved for public release by DEVCOM Soldier Center: PAO# PR2022\_26340. This work was supported in part by NSF DMR 2018326 and 1740795 awards and by the US Army DEVCOM Soldier Center AA1 basic research program. AMF was supported by the NSF NRT-HDR 2021871 fellowship. VN was supported by CSIR-NCL lab funds. The authors also thank Ronald L. Grimm and Julia Martin for helpful discussions.

#### **Conflict of Interest**

The authors declare no conflict of interest.

#### **Data Availability Statement**

The data that support the findings of this study are available from the corresponding author upon reasonable request.

#### **Keywords**

2D properties, MXenes, optical properties, plasmons, ultrafast spectroscopy

Received: September 20, 2022 Revised: October 26, 2022 Published online: December 22, 2022

- M. Lukatskaya, S. Kota, Z. Lin, M.-Q. Zhao, N. Shipgel, D. M. Levi, J. Halim, P. L. Taberna, M. W. Barsoum, P. Simon, Y. Gogotsi, *Nat. Energy* 2017, 2, 17105.
- [2] A. D. Dillon, M. Ghidiu, A. Krick, J. Griggs, S. J. May, Y. Gogotsi, M. W. Barsoum, A. T. Fafarman, Adv. Funct. Mater. 2016, 26, 4162.
- [3] B. Anasori, Y. Xie, M. Beidaghi, J. Lu, B. C. Hosler, L. Hultman, P. R. Kent, Y. Gogotsi, M. W. Barsoum, ACS Nano 2015, 9, 9507.
- [4] M. Naguib, V. N. Mochalin, M. W. Barsoum, Y. Gogotsi, Adv. Mater. 2014, 26, 992.
- [5] M. Ghidiu, M. R. Lukatskaya, M. Q. Zhao, Y. Gogotsi, M. W. Barsoum, *Nature* 2014, 516, 78.

- [6] M. Naguib, O. Mashtalir, J. Carle, J. Lu, L. Hultman, Y. Gogotsi, M. W. Barsoum, ACS Nano 2012, 6, 1322.
- [7] G. Li, N. Amer, H. A. Hafez, S. Huang, D. Turchinovich, V. N. Mochalin, F. A. Hegmann, L. V. Titova, *Nano Lett.* 2020, 20, 636.
- [8] G. Li, V. Natu, T. Shi, M. W. Barsoum, L. V. Titova, ACS Appl. Energy Mater. 2020, 3, 1530.
- [9] F. Shahzad, M. Alhabeb, C. B. Hatter, B. Anasori, S. Man Hong, C. M. Koo, Y. Gogotsi, Science 2016, 353, 1137.
- [10] M. Han, C. E. Shuck, R. Rakhmanov, D. Parchment, B. Anasori, C. M. Koo, G. Friedman, Y. Gogotsi, ACS Nano 2020, 14, 5008.
- [11] J. Lipton, J. A. Röhr, V. Dang, A. Goad, K. Maleski, F. Lavini, M. Han, E. H. R. Tsai, G.-M. Weng, J. Kong, E. Riedo, Y. Gogotsi, A. D. Taylor, *Matter* 2020, 3, 546.
- [12] G. Li, K. Montazeri, M. K. Ismail, M. W. Barsoum, B. Nabet, L. V. Titova, Adv. Photonics Res. 2020, 1, 2000084.
- [13] D. B. Velusamy, J. K. El-Demellawi, A. M. El-Zohry, A. Giugni, S. Lopatin, M. N. Hedhili, A. E. Mansour, E. D. Fabrizio, O. F. Mohammed, H. N. Alshareef, Adv. Mater. 2019, 31, 1807658.
- [14] L. M. Wu, X. T. Jiang, J. L. Zhao, W. Y. Liang, Z. J. Li, W. C. Huang, Z. T. Lin, Y. Z. Wang, F. Zhang, S. B. Lu, Y. J. Xiang, S. X. Xu, J. Q. Li, H. Zhang, Laser Photonics Rev. 2018, 12, 10.
- [15] C. Wang, Q. Peng, X. W. Fan, W. Y. Liang, F. Zhang, J. Liu, H. Zhang, Chinese Phys. B 2018, 27, 4.
- [16] K. Maleski, C. E. Shuck, A. T. Fafarman, Y. Gogotsi, Adv. Opt. Mater. 2021, 9, 2001563.
- [17] M. Han, K. Maleski, C. E. Shuck, Y. Yang, J. T. Glazar, A. C. Foucher, K. Hantanasirisakul, A. Sarycheva, N. C. Frey, S. J. May, V. B. Shenoy, E. A. Stach, Y. Gogotsi, J. Am. Chem. Soc. 2020, 142, 19110.
- [18] H. Li, S. Chen, D. W. Boukhvalov, Z. Yu, M. G. Humphrey, Z. Huang, C. Zhang, ACS Nano 2022, 16, 394.
- [19] D. Zhang, D. Shah, A. Boltasseva, Y. Gogotsi, ACS Photonics 2022, 9, 1108.
- [20] A. Olshtrem, S. Chertopalov, O. Guselnikova, R. R. Valiev, M. Cieslar, E. Miliutina, R. Elashnikov, P. Fitl, P. Postnikov, J. Lancok, V. Svorcik, O. Lyutakov, 2D Mater. 2021, 8, 045037.
- [21] K. Chaudhuri, M. Alhabeb, Z. Wang, V. M. Shalaev, Y. Gogotsi, A. Boltasseva, ACS Photonics 2018, 5, 1115.
- [22] V. Pacheco-Peña, T. Hallam, N. Healy, Light: Sci. Appl. 2022, 11, 22.
- [23] D. Xu, Z. Li, L. Li, J. Wang, Adv. Funct. Mater. 2020, 30, 2000712.
- [24] A. D. Dillon, M. J. Ghidiu, A. L. Krick, J. Griggs, S. J. May, Y. Gogotsi, M. W. Barsoum, A. T. Fafarman, Adv. Funct. Mater. 2016, 26, 4162.
- [25] H. Kim, B. Anasori, Y. Gogotsi, H. N. Alshareef, Chem. Mater. 2017, 29, 6472.
- [26] R. Li, L. Zhang, L. Shi, P. Wang, ACS Nano 2017, 11, 3752.
- [27] H. Lin, S. Gao, C. Dai, Y. Chen, J. Shi, J. Am. Chem. Soc. 2017, 139, 16235.
- [28] L. V. Besteiro, P. Yu, Z. Wang, A. W. Holleitner, G. V. Hartland, G. P. Wiederrecht, A. O. Govorov, *Nano Today* 2019, 27, 120.
- [29] G. V. Hartland, L. V. Besteiro, P. Johns, A. O. Govorov, ACS Energy Lett. 2017, 2, 1641.
- [30] G. V. Hartland, Chem. Rev. 2011, 111, 3858.
- [31] Y. Huang, J. Zhou, G. Wang, Z. Sun, J. Am. Chem. Soc. 2019, 141, 8503.
- [32] A. Sarycheva, T. Makaryan, K. Maleski, E. Satheeshkumar, A. Melikyan, H. Minassian, M. Yoshimura, Y. Gogotsi, J. Phys. Chem. C 2017, 121, 19983.
- [33] P. U. Jepsen, D. G. Cooke, M. Koch, Laser Photonics Rev. 2011, 5, 124.
- [34] J. H. Hodak, A. Henglein, G. V. Hartland, Pure Appl. Chem. 2000, 72, 189.
- [35] R. H. M. Groeneveld, R. Sprik, A. Lagendijk, *Phys. Rev. B* **1995**, *51*, 11433.
- [36] M. L. Brongersma, N. J. Halas, P. Nordlander, Nat. Nanotechnol. 2015, 10, 25.
- [37] S. L. Logunov, T. S. Ahmadi, M. A. El-Sayed, J. T. Khoury, R. L. Whetten, J. Phys. Chem. B 1997, 101, 3713.





www.advmat.de

- [38] S. Link, C. Burda, M. B. Mohamed, B. Nikoobakht, M. A. El-Sayed, Phys. Rev. B 2000, 61, 6086.
- [39] J. Hohlfeld, S. S. Wellershoff, J. Güdde, U. Conrad, V. Jähnke, E. Matthias, Chem. Phys. 2000, 251, 237.
- [40] B. T. Diroll, S. Saha, V. M. Shalaev, A. Boltasseva, R. D. Schaller, Adv. Opt. Mater. 2020, 8, 2000652.
- [41] L. Chen, X. Shi, N. Yu, X. Zhang, X. Du, J. Lin, Materials 2018, 11, 1701.
- [42] H. Gholivand, S. Fuladi, Z. Hemmat, A. Salehi-Khojin, F. Khalili-Araghi, J. Appl. Phys. 2019, 126, 065101.
- [43] L. Chen, X. Shi, N. Yu, X. Zhang, X. Du, J. Lin, Materials (Basel) 2018, 11, 1701.
- [44] Z. Guo, N. Miao, J. Zhou, Y. Pan, Z. Sun, Phys. Chem. Chem. Phys. 2018, 20, 19689.
- [45] D. M. Monahan, L. Guo, J. Lin, L. Dou, P. Yang, G. R. Fleming, J. Phys. Chem. Lett. 2017, 8, 3211.
- [46] Q. Sun, J. Gong, X. Yan, Y. Wu, R. Cui, W. Tian, S. Jin, Y. Wang, Nano Lett. 2022, 22, 2995.

- [47] G. Li, K. Kushnir, Y. Dong, S. Chertopalov, A. M. Rao, V. N. Mochalin, R. Podila, L. V. Titova, 2D Mater. 2018, 5, 035043
- [48] W. Zheng, B. Sun, D. Li, S. M. Gali, H. Zhang, S. Fu, L. Di Virgilio, Z. Li, S. Yang, S. Zhou, D. Beljonne, M. Yu, X. Feng, H. I. Wang, M. Bonn, *Nat. Phys.* 2022, *18*, 544.
- [49] G. Li, N. Li, S. Peng, B. He, J. Wang, Y. Du, W. Zhang, K. Han, F. Dang, Adv. Energy Mater. 2021, 11, 2002721.
- [50] Y. Shao, F. Zhang, X. Shi, H. Pan, Phys. Chem. Chem. Phys. 2017, 19, 28710.
- [51] J. Halim, I. Persson, E. J. Moon, P. Kuhne, V. Darakchieva, P. O. A. Persson, P. Eklund, J. Rosen, M. W. Barsoum, J Phys Condens Matter 2019, 31, 165301.
- [52] B. Anasori, C. Shi, E. J. Moon, Y. Xie, C. A. Voigt, P. R. C. Kent, S. J. May, S. J. L. Billinge, M. W. Barsoum, Y. Gogotsi, *Nanoscale Horiz*. 2016, 1, 227.
- [53] J. Halim, E. J. Moon, P. Eklund, J. Rosen, M. W. Barsoum, T. Ouisse, Phys. Rev. B 2018, 98, 104202.

Adv. Mater. 2023, 35, 2208659